

Mesons versus quasi-normal modes: undercooling and overheating

Angel Paredes¹, Kasper Peeters¹ and Marija Zamaklar²

¹*Institute for Theoretical Physics, Utrecht University, P.O. Box 80.195, 3508 TD Utrecht, The Netherlands.*

²*Department of Mathematical Sciences, Durham University, South Road, Durham DH1 3LE, United Kingdom.*

a.paredesgalan@uu.nl
kasper.peeters@aei.mpg.de
marija.zamaklar@durham.ac.uk

ABSTRACT: In holographic models of gauge theories with matter, there generically exists a first order phase transition in which mesons dissociate. We perform a careful analysis of the meson and quasi-particle spectra in the overheated resp. undercooled regimes close to the junction of the two phases. We show that all overheated finite meson masses eventually become infinitely degenerate, which implies that any connection to the quasi-particle spectrum is more subtle than previously suggested. For the Sakai-Sugimoto model no smooth connection between these spectra is possible.

KEYWORDS: AdS/CFT, mesons, phase transitions.

Contents

1. Introduction	1
2. Setup and numerical motivation	3
3. The D3/D7 system	6
3.1 Zero-temperature potentials	6
3.2 Brane embeddings in the Rindler approximation	7
3.3 Structure of the Schrödinger potentials	8
3.4 Meson and quasi-normal modes	13
4. The D4/D8 system	14
4.1 Schrödinger potentials	14
4.2 Mesons and quasi-normal modes	17
5. Conclusions and discussion	18
A. Appendix	19
A.1 Coordinate frames	19
A.2 Quasinormal frequencies in toy potentials	20

1. Introduction

Holographic models for gauge theories with matter exhibit a rather generic three-phase structure. For low temperatures, the background is a regular geometry, representing the confined phase of the gauge theory. At sufficiently high temperature, the background undergoes a Hawking-Page transition to a black brane geometry. In the dual gauge theory, this transition corresponds to the deconfinement of gluons. Mesons still remain bound, as long as the brane representing the matter degrees of freedom does not intersect the background horizon. When this finally happens, a second transition occurs, to a phase in which mesons melt and the gauge theory is fully deconfined. We will call these three phases the low, intermediate and high temperature phase respectively.¹

After the mesons have melted, one is left with a strongly-coupled quark-gluon fluid. This fluid exhibits a discrete spectrum of unstable excitations [4], which are described by quasi-normal modes on the probe brane. It has been suggested [5, 6] that the thermal pole

¹There is by now a large list of references dealing with this three-phase structure; seminal papers are [1] for the D3/D7 system, [2] for the D4/D6 case and [3] for the D4/D8 model. In special situations the intermediate phase can be absent, but we will not discuss those cases here.

masses of mesons before the transition should be related to the real parts of the quasi-normal modes after the transition. It would then be possible to follow the stable mesons of the intermediate temperature phase into the high-temperature phase, where they become unstable quasi-particles with finite decay width. The fact that the widths are of order one is consistent with the expected behaviour of meson decay widths in the deconfined phase.² Moreover, lattice results indicate that finite-width mesonic resonances indeed survive above the deconfinement temperature (see e.g. [8, 9]).

While such a connection between stable and unstable meson modes thus seems reasonable, it so far relies on numerical evidence. Other known facts about the generic thermal behaviour of meson masses suggest that the connection might be more subtle. In the intermediate temperature phase, the pole masses of mesons are known to decrease as the temperature goes up [10]. This shows qualitative resemblance with lattice QCD studies [11, 12]. In QCD proper, chiral partners such as the ρ and a_1 meson eventually become degenerate when chiral symmetry is restored. In contrast, all holographic models go through the first-order meson melting phase transition before such degeneracies can be observed. However, the graphs of the thermal behaviour of the masses [10] suggest that a degeneracy may still occur when the system is overheated. If such a degeneracy occurs, then an identification of the discrete spectrum before and after the transition becomes more subtle (we will indeed see that this happens).

A further problem occurs in the Sakai-Sugimoto model with zero bare quark mass. The embeddings after the transition are all equivalent, which implies that the quasi-normal mode spectrum after the transition is fixed, i.e. it never becomes degenerate. If the meson spectrum, on the other hand, does become degenerate at the junction, then no smooth identification seems possible. In addition,³ mesons of this model transform under the adjoint of the diagonal $SU(N_f)$, while the quasi-normal modes sit in the adjoint of $SU(N_f)_L$ or $SU(N_f)_R$. This again makes a straightforward identification of the spectra unlikely.

In the present paper we therefore try to answer two key questions: what is the precise behaviour of meson pole masses as the critical embedding is approached from below the transition temperature, and does this leave any room for a connection to the real parts of the frequencies of the quasi-normal modes just above the critical temperature? We will restrict ourselves to an analysis of the spectrum of *vector* excitations close to the critical embedding, and comment only briefly on a similar analysis for scalar excitations. For the sake of simplicity, we will also only consider modes homogeneous in the internal spheres; generalisation to other cases should be straightforward.

We will first provide numerical evidence which indicates that the potential of the associated Schrödinger problem takes a particularly simple form as the critical embedding is approached. Inspired by these numerical results, we then present an analytic procedure to compute the spectrum close to either side of the phase transition. We will show that

²In the intermediate-temperature phase the decay of a meson to a quark-antiquark pair would also be of order one, but because mesons are anomalously light (of order $2m_q/\sqrt{\lambda}$ where m_q is the constituent quark mass), there is no phase space available for their decay. Meson to two-meson decays [7] are of order $1/N_c$.

³We thank Ofer Aharony for emphasising this point to us.

any finite number of mesons in the discrete spectrum of the intermediate phase become degenerate in mass at the critical (overheated) embedding (our findings avoid the no-crossing theorem of Von Neumann & Wigner [13] because a finite change in the temperature leads to an infinite change of the potential).

A similar degeneracy occurs, but only in the D3/D7 case and the polar embedding of the D4/D6 systems (see figure 1), for the quasi-normal frequencies when the critical embedding is approached from the high-temperature side (undercooled). Since the masses and quasi-normal modes are labelled by a single excitation number n , there is in principle an infinite number of ways to relate the states in these two spectra, and the connection between mesons and quasi-normal modes thus seems more subtle than previously suggested [5, 6]. For the D4/D8 and equatorial D4/D6 systems, the quasi-normal modes never degenerate, and there is thus no smooth connection to the meson spectrum.

2. Setup and numerical motivation

Before we discuss our main analytic results for the behaviour of the meson spectrum near the melting transition, let us first set the stage and motivate our approach by some numerical results.

Our starting point is the generic expression for the background metric of a Dp -brane. It is given by

$$ds^2 = \left(\frac{u}{L}\right)^{\frac{7-p}{2}} \left(-f_p(u)dt^2 + \delta_{ij}dx^i dx^j\right) + \left(\frac{u}{L}\right)^{\frac{p-7}{2}} \left(\frac{du^2}{f_p(u)} + u^2 d\Omega_{8-p}^2\right), \quad (2.1)$$

where $i, j = 1 \dots p$ and $f_p(u) = 1 - (u_T/u)^{7-p}$. There is also a non-trivial dilaton

$$e^{-\phi} = \left(\frac{u}{L}\right)^{(p-7)(p-3)/4}. \quad (2.2)$$

The temperature of this background is given by

$$T = \frac{7-p}{4\pi L} \left(\frac{u_T}{L}\right)^{\frac{5-p}{2}}. \quad (2.3)$$

Probe branes can be embedded in various ways, depending on the value of p . In all cases which we will discuss, four of the directions of the probe brane are aligned with t and three of the x^i . For the D4/D6 system one has a choice of two different subspaces for the embedding of the probe. One of these occurs again for the D3/D7 system and the other one occurs for the D4/D8 system. See figure 1 for details.

There are two types of embeddings of the probe brane, depending on whether or not it intersects the horizon of the background. The ‘‘Minkowski embeddings’’ do not reach the horizon. The non-equatorial embeddings of this type are described most conveniently in the r - λ coordinate system using the λ coordinate on the world-volume. The ‘‘black hole embeddings’’, on the other hand, do reach the black hole horizon, intersecting it orthogonally. The non-equatorial embeddings of this type are best described in a polar coordinate

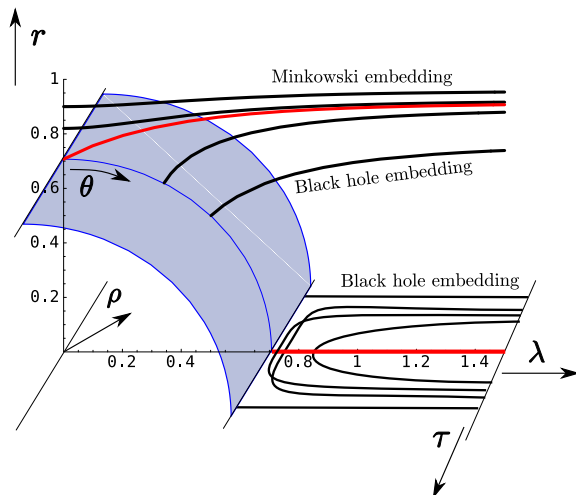


Figure 1: The generic holographic setup for the D4/D6 system. The r - λ plane is a conformally flat plane arising from the second term in (2.1), and $\tau \equiv x^4$ (see the appendix for details). The embeddings in the horizontal τ - λ plane will be called “equatorial”. The embeddings of the D4/D8 system are similar to these equatorial ones. The D3/D7 system only has embeddings corresponding to the ones in the vertical r - λ plane, which we will call “polar”. Critical embeddings are displayed in red, while the horizon is indicated by the blue surface.

system ρ - θ , as indicated in figure 1 (see appendix A.1 for details on our coordinate systems). The embedding which lies along the horizontal axis plays a special role, as it occurs in all models which we analyse here.

Statements concerning a possible relation between meson modes and quasi-normal modes have all been concerned with the behaviour of embeddings in the r - λ plane, in other words, with the D3/D7 and D4/D6 system. There is, however, also a critical embedding separating a Minkowski from a black hole phase in the D4/D8 system, i.e. in the τ - λ plane. We will analyse this system separately in section 4.

Let us now turn to the vector fluctuations on the probe branes. The equations governing them follow from an expansion of the induced action in powers of the abelian field strength. At lowest order one has

$$S_{\text{vector}} \propto \int d^4x d\lambda d\Omega_{6-p} e^{-\phi} \sqrt{-\hat{g}} F_{MN} F_{PQ} \hat{g}^{MP} \hat{g}^{NQ}, \quad (2.4)$$

(and similar for the ρ - θ and τ - λ system) where \hat{g} denotes the induced metric. The spatial components of the fields which describe the massive vector mesons arise from the expansion

$$F_{0a} = \sum_n \partial_0 B_a^{(n)} \psi_{(n)}(\lambda), \quad F_{\lambda a} = \sum_n B_a^{(n)} \partial_\lambda \psi_{(n)}(\lambda). \quad (2.5)$$

We will focus solely on thermal pole masses of the vector mesons, which are defined by $\partial_0^2 B_a^{(n)} = -m_{(n)}^2 B_a^{(n)}$. The equation of motion for the modes $\psi_{(n)}$ which then follows reads

$$\partial_\lambda \left[e^{-\phi} \sqrt{-\hat{g}} \hat{g}^{aa} \hat{g}^{\lambda\lambda} \partial_\lambda \psi_{(n)} \right] + m_{(n)}^2 e^{-\phi} \sqrt{-\hat{g}} \hat{g}^{aa} \hat{g}^{00} \psi_{(n)} = 0. \quad (2.6)$$

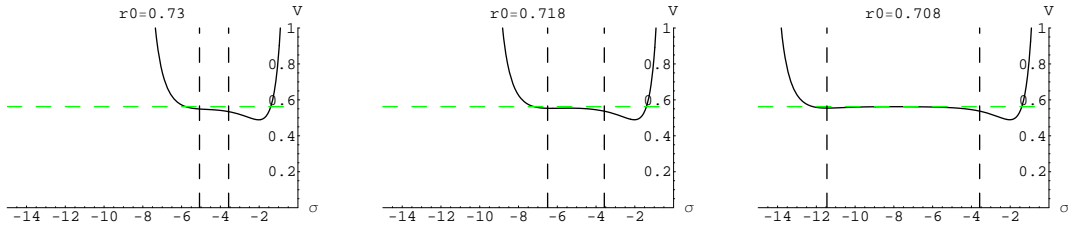


Figure 2: The Schrödinger potential for Minkowski embeddings in the D3/D7 system, close to criticality, for various values r_0 of the intersection with the vertical axis. The green dashed line indicates the asymptotic potential in the box, given by (3.17); the vertical dashed lines mark the edges of the plateau (which will be defined in section 3.3).

These equations can be solved in a series expansion near the tip of the brane, and then extended numerically using standard shooting methods. In the Minkowski phase, the discrete mass spectrum arises after imposing that the fluctuations are regular in the IR and normalisable in the UV. In the black hole phase, the discrete quasinormal spectrum comes from incoming boundary conditions in the IR and normalisability in the UV.

In order to get a better insight into the structure of the spectrum, it is useful to perform a coordinate transformation and a wave function rescaling which brings (2.6) in Schrödinger form. Following the notation of [14], we write the equation in the general form

$$\frac{1}{\Gamma(\lambda)} \partial_\lambda \left[\frac{\Gamma(\lambda)}{\Sigma^2(\lambda)} \partial_\lambda \psi_{(n)} \right] + m_n^2 \psi_{(n)} = 0. \quad (2.7)$$

(The functions Γ and Σ of course implicitly depend on the probe brane embedding function $r(\lambda)$). By introducing a new coordinate and a rescaled wave function according to

$$\frac{d\lambda}{d\sigma} = \frac{1}{\Sigma}, \quad \tilde{\psi}_{(n)} = \Xi \psi_{(n)}, \quad \Xi = \sqrt{\frac{\Gamma}{\Sigma}}, \quad (2.8)$$

the problem is transformed into a Schrödinger type problem,

$$-\partial_\sigma^2 \tilde{\psi}_{(n)} + V \tilde{\psi}_{(n)} = E_n \tilde{\psi}_{(n)}, \quad \text{with} \quad V = \frac{\partial_\sigma^2 \Xi}{\Xi}, \quad E_n = m_n^2. \quad (2.9)$$

We will see how to approximate the potential V analytically in the following sections. However, to get an idea of what we are aiming for, let us first give the results of a numerical analysis, valid for the embeddings in the r - λ plane.

The resulting potential for the Minkowski embedding is displayed in figure 2, where r_0 is the position at which the probe brane intersects the vertical axis of figure 1. The σ coordinate is bounded on both sides. As the critical embedding is approached, the potential becomes more and more rectangular, while the box size (i.e. the range of σ) grows, until it eventually becomes unbounded.

The result for the black hole embedding is shown in figure 3, where $\chi_0 = \cos \theta_0$ is related to the value of the angular coordinate at which the brane intersects the horizon, as shown in figure 1. Now the σ coordinate is bounded only in the UV direction, and the potential develops a clear step-shape. As the critical embedding is approached, the step becomes infinitely long.

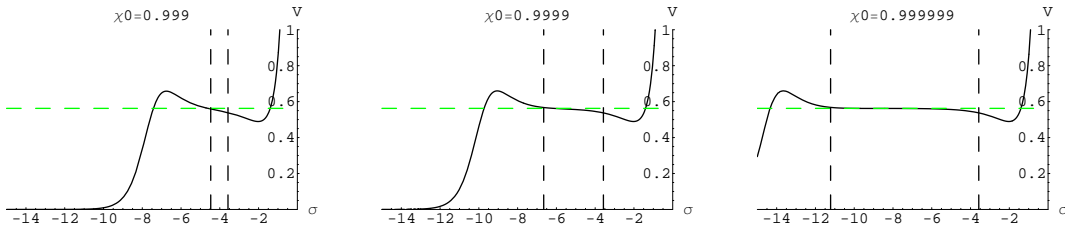


Figure 3: The Schrödinger potential for black hole embeddings in the D3/D7 system, close to criticality, for various values of the angle χ_0 of intersection with the horizon. Green and black dashed lines have the same meaning as in 2.

These figures suggest that it should be possible to find a simple description of the potential very close to the critical embedding. We will do that in the next section. A somewhat similar story holds true for the D4/D8 embeddings, which we will analyse in more detail in section 4.

3. The D3/D7 system

3.1 Zero-temperature potentials

Before giving our analytic results at finite temperature, it is instructive to recall the structure of the Schrödinger potential at zero temperature. Although we mainly focus on the D3/D7 system ($p = 3$), we have kept part of the discussion general so the D4/D6 system can be obtained (by setting $p = 4$). At zero temperature, there are two types of embeddings. One is the conformal embedding of the D7-brane (when the constituent quark mass m_q is zero), and the other one is the non-conformal embedding, when $m_q \neq 0$. In the former case the induced metric on the worldvolume of the brane is exactly that of $\text{AdS}_5 \times S^3$, while in the latter case the induced metric approaches this only in the UV, i.e. near the AdS boundary. The embedding is trivial in these cases, given by $r = m_q$, which leads to the vector fluctuation equation [15]⁴

$$\frac{1}{\lambda^3} \partial_\lambda \left(\lambda^3 \partial_\lambda \psi_{(n)} \right) + \frac{m_{(n)}^2}{(\lambda^2 + m_q^2)^2} \psi_{(n)} = 0. \quad (3.1)$$

The Schrödinger potentials for the $m_q = 0$ and $m_q > 0$ are easily computed to be,

$$V_{m_q=0}(\sigma) = \frac{3}{4\sigma^2}, \quad \lambda = -\sigma^{-1}, \quad (3.2)$$

$$V_{m_q \neq 0}(\sigma) = m_q^2 \left[\frac{1}{2} + \frac{3}{4} \left(\tan^2(m_q \sigma) + \frac{1}{\tan^2(m_q \sigma)} \right) \right], \quad \lambda = m_q \tan(m_q \sigma).$$

In the conformal case the potential goes to a constant (zero) in the IR, while it diverges in the UV. In the non-conformal case, the potential diverges both in the UV and IR. The

⁴The curvature radius L has been set to one, hence the m_q variable has dimension length. The coordinates used are $r = u \cos \theta$ and $\lambda = u \sin \theta$ as in [15], but different from the coordinates of appendix A.1.

box shape of the potential $V_{m_q \neq 0}$ obviously leads to a discrete spectrum, in contrast to the continuum spectrum of the conformal case. If one replaces $V_{m_q \neq 0}$ with an infinitely high box of size $\pi/(2m_q)$, the spectrum asymptotically becomes $m_{(n)}^2 = 4m_q^2 n^2$, in agreement with the large- n limit of the exact spectrum found in [15]. Hence, we see that while in the UV both branes are the same (i.e. AdS), with a diverging potential, the main difference between the two comes from the IR, i.e. from near the Poincaré horizon.

Let us now turn to the $T \neq 0$ case. In this case the analytic form of the embeddings of the branes is unknown, and so one would perhaps expect the analysis to be more complicated than above. However, the key element is that, for branes close to the critical embedding, only the near horizon region of the background is relevant, a region which is quite different from the $T = 0$ background discussed above. Brane embeddings near the horizon were analysed by [16, 17]. As we will show below, when we get closer and closer to the critical embedding, the region in Schrödinger coordinate which corresponds to the near-horizon region becomes larger and larger, growing without bound. In the strict limit, we end up with an extremely simple, flat potential of infinite length, only corrected by finite-size effects whose relative effect scales to zero. The simple potential then allows us to make an exact statement about the spectrum.

3.2 Brane embeddings in the Rindler approximation

Having illustrated the behaviour of the Schrödinger potential with some numerical results and having sketched our approach, let us now provide an analytic argument which will lead to an exact potential in the critical limit. We first need to summarise the brane embeddings close to the horizon. As in [17], we write the metric of the $8 - p$ sphere as

$$d\Omega_{8-p}^2 = d\theta^2 + \sin^2 \theta d\Omega_{6-p}^2 + \cos^2 \theta d\varphi^2. \quad (3.3)$$

We will consider the probe embedding extended in three x -directions, wrapping the $6 - p$ sphere at fixed φ and having non-trivial $\theta(r)$. We now want to zoom in a region near the horizon, for a brane which is near its critical embedding. This means a region close to $\theta = 0$, $r = r_0$. Let us choose a parametrisation

$$u = u_T + \pi T z^2, \quad \theta = \frac{y}{L} \left(\frac{L}{u_T} \right)^{\frac{p-3}{4}}, \quad \tilde{x} = \left(\frac{u_T}{L} \right)^{\frac{7-p}{4}} x. \quad (3.4)$$

Then, considering the limit where

$$\frac{u - u_T}{u_T} = \frac{\pi T z^2}{u_T} \ll 1, \quad \theta = \frac{y}{L} \left(\frac{L}{u_T} \right)^{\frac{p-3}{4}} \ll 1, \quad (3.5)$$

we find Rindler space ⁵

$$ds^2 = -(2\pi T)^2 z^2 dt^2 + dz^2 + dy^2 + y^2 d\Omega_{6-p}^2 + d\tilde{x}_3^2 + \dots, \quad (3.6)$$

⁵The relation with the ρ, χ variables of figure 1 is, for the D3/D7 system, given by $\rho - 1 = z/L$, $\chi = 1 - \frac{1}{2}y^2/L^2$, valid near $\rho \approx 1$, $\chi \approx 1$; see appendix A.1 for details.

while the dilaton approaches a constant. Notice the horizon is now at $z = 0$. The Rindler approximation ceases to be valid at distances set by

$$R_{\text{Rindler}} \equiv \sqrt{\frac{u_T}{\pi T}} = \begin{cases} L & p = 3; \\ \frac{2}{\sqrt{3}} (u_T L^3)^{1/4} & p = 4. \end{cases} \quad (3.7)$$

The equation describing the probe embedding $y(z)$ in this region is

$$zy\ddot{y} + (y\dot{y} - (6-p)z)(1 + \dot{y}^2) = 0. \quad (3.8)$$

An important aspect of (3.8) is its scaling symmetry, $z \rightarrow \lambda z$, $y \rightarrow \lambda y$. This means that changing z_0 or y_0 does not really influence the shape of the embedding but just rescales it.

The obvious solution of this equation gives the critical embedding,

$$y_{\text{crit}} = \sqrt{6-p} z. \quad (3.9)$$

If the brane does not touch the horizon, there is a family of smooth Minkowski embeddings parametrised by z_0 , the distance of the tip of the brane to the horizon. The solution near $z = z_0$ reads

$$y_{\text{Mink}} = z_0 \left[\sqrt{2(7-p)} \sqrt{\frac{z-z_0}{z_0}} + \mathcal{O}\left(\left(\frac{z-z_0}{z_0}\right)^{\frac{3}{2}}\right) \right]. \quad (3.10)$$

For $z \gg z_0$ one can find the asymptotic solution [16] which shows that the embedding approaches the critical one y_{crit} up to corrections which scale as a negative power of z . Taking the limit $z_0 \rightarrow 0$ corresponds to approaching the critical embedding.⁶ If the brane intersects the horizon, there is a family of black hole embeddings parametrised by y_0 , which near $z = 0$ reads

$$y_{\text{BH}} = y_0 \left[1 + \frac{6-p}{4} \frac{z^2}{y_0^2} + \mathcal{O}\left(\left(\frac{z}{y_0}\right)^3\right) \right]. \quad (3.11)$$

Again, the parameter y_0 measures the deviation from the critical embedding, and taking the limit $y_0 \rightarrow 0$ corresponds to the limit in which the critical embedding is reached. In the other regime $z \gg z_0$ the embedding again approaches the critical one [16].

3.3 Structure of the Schrödinger potentials

Let us now analyse the Schrödinger potentials for the spectrum of vector meson fluctuations. The dominant part of the potential will turn out to be located in the Rindler region, so we will first focus on the embeddings described in the previous subsection.⁷ We will focus on a simple subset of the possible excitations, namely those described (in the $A_0 = 0$ gauge) by $A_i = e^{-i\omega t} \psi(z)$. In Rindler coordinates, the equation for the fluctuation is

$$\partial_z \left(y^{6-p} z (1 + \dot{y}^2)^{-\frac{1}{2}} \partial_z \psi \right) + \frac{y^{6-p}}{z} (1 + \dot{y}^2)^{\frac{1}{2}} \tilde{\omega}^2 \psi = 0, \quad (3.12)$$

⁶However, note that the limit is subtle. Since the expansion parameter is $(z - z_0)/z_0$ one cannot first take $z_0 \rightarrow 0$, but rather one has to simultaneously scale $z \rightarrow 0$. This is similar to the situation we had for the $T = 0$ embedding and the limit $m_q \rightarrow 0$.

⁷Several other properties of holographic QCD are also fully determined by the Rindler region; see e.g. [18].

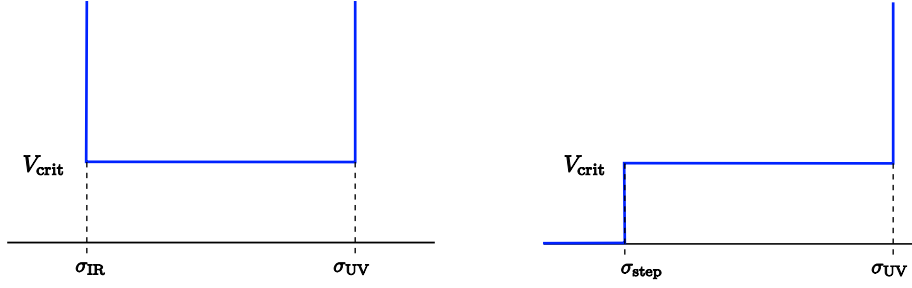


Figure 4: The approximations used for the potentials close to the critical embedding, to be compared with the exact numerical results in figure 2 and 3.

where $\tilde{\omega} \equiv \frac{\omega}{2\pi T}$. Using (3.8) this equation can be written as

$$\partial_z^2 \psi + \frac{1 + \dot{y}^2}{z} \partial_z \psi + \frac{1 + \dot{y}^2}{z^2} \tilde{\omega}^2 \psi = 0. \quad (3.13)$$

The IR boundary conditions to be imposed on the wave function ψ are regularity in the Minkowski case and incoming boundary conditions in the black hole case,

$$\psi_{\text{Mink}} = 1 + \mathcal{O}(z - z_0), \quad \psi_{\text{bh}} = z^{-i\tilde{\omega}} (1 + \mathcal{O}(z)). \quad (3.14)$$

It is useful to recast equation (3.12) in Schrödinger form, as we did for the full problem in the previous section. In terms of the notation used in [14] we now have

$$\Gamma = \frac{y^{6-p}}{z} (1 + \dot{y}^2)^{\frac{1}{2}}, \quad \Sigma = \frac{(1 + \dot{y}^2)^{\frac{1}{2}}}{z}, \quad \Xi = y^{\frac{6-p}{2}}, \quad \tilde{\psi} = \Xi \psi. \quad (3.15)$$

The new radial variable σ is defined through $d\sigma/dz = \Sigma$, as before. With these redefinitions, equation (3.12), describing fluctuations in the IR, can be rewritten as

$$-\partial_\sigma^2 \tilde{\psi} + V_{\text{IR}} \tilde{\psi} = \tilde{\omega}^2 \tilde{\psi}, \quad \text{with} \quad V_{\text{IR}} = \frac{\partial_\sigma^2 \Xi}{\Xi} = \frac{(6-p) z^2}{2y^2} \frac{6-p + ((6-p)/2 - 1)(\partial_z y)^2}{1 + (\partial_z y)^2}. \quad (3.16)$$

Using the explicit solutions for brane embeddings, described in the previous subsection, we can compute the potentials. They are plotted in figure 6 for the $p = 3$ case.

Let us first discuss the potential for the critical embedding (3.9). It turns out to be constant everywhere in the Rindler region, with a value given by

$$V_{\text{crit}}^{\text{IR}} = \frac{(6-p)^2}{4(7-p)}. \quad (3.17)$$

The σ coordinate is related to the z coordinate by $\sigma = \sqrt{7-p} \log z$, so the point $z = 0$ is mapped to $\sigma = -\infty$ while the edge of the Rindler region in the UV is mapped to $\sigma = +\infty$. The potential for the critical embedding is thus a constant on $\sigma = \langle -\infty, +\infty \rangle$.⁸

⁸If one repeats the computation for a scalar excitation $y = y_{\text{cl}}(z) + \delta y(t, z)$, one gets for the critical embedding $V_{\text{crit}} = \frac{p^2 - 8p + 8}{4(7-p)^2}$ which is negative for the cases of interest $p = 3, 4$, signalling unambiguously the appearance of scalar tachyons in this channel near the critical embedding. These tachyonic modes were first explicitly discussed in [19].

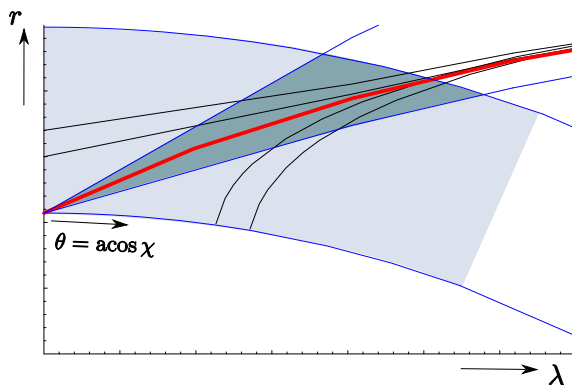


Figure 5: Schematic indication of the three regions defined in the text. The light shaded area is the Rindler region. For a fixed embedding, the segment before entering the dark shaded area is the “deep IR”, the segment after exiting is the “UV” while the segment inside the dark shaded area is the “intermediate IR”. The latter grows, in the Schrödinger coordinate, as $-2 \log(r_0 - 1/\sqrt{2})$ or $-\log(1 - \chi_0)$.

We have already seen numerical evidence for the formation of this plateau both from the Minkowski side as well as from the black hole side (figure 2 and 3). In the Minkowski case, the plateau arises from an approximately square well, while in the black hole case it arises from a step-like potential (note that the step is a generic feature of black hole embeddings [20]). We thus want to approximate these potentials as in figure 4.⁹ Using the results of the present section, we can now make explicit how the *lengths* of the long flat segments of these potentials depend on the *distance* to the critical embedding.

For all embeddings, three regions can be distinguished. First, there is a “deep IR region”, where the near-critical Minkowski and near-critical black hole embeddings still deviate from the critical embedding. Somewhat further out, but still in the region where the Rindler approximation makes sense, there is an “intermediate IR region” or “plateau”. In this region the embeddings are well-approximated by the critical embedding. Finally, for $z \approx R_{\text{Rindler}}$, we leave the regime of validity of the Rindler approximation, and we have no analytic control anymore over the shape of the embeddings in this “UV region”. The three regions are shown in figure 5.

The potential in the intermediate IR region is essentially constant, because the brane is there almost the same as the critical one. The key observation is that, as we argue below, the size of this intermediate region in the Schrödinger coordinate diverges logarithmically as the critical embedding is approached. The other two regions (“deep IR” and “UV region”), on the other hand, have a size which is independent of z_0 or y_0 . Hence, as observed numerically, when we approach the critical embedding (either from the black hole or from the Minkowski side) the Schrödinger potential becomes constant, due to the fact that the size of the intermediate IR region in the Schrödinger coordinate diverges.

⁹For Minkowski embeddings in the D4/D6 case, the Schrödinger potential does not diverge at $z = z_0$ but goes to a finite constant. However, regularity of the fluctuation requires $\tilde{\psi}$ to vanish at the finite value $\sigma_{\text{IR}} = \sigma(z = z_0)$. Thus, a box potential is also a good approximation in this case.

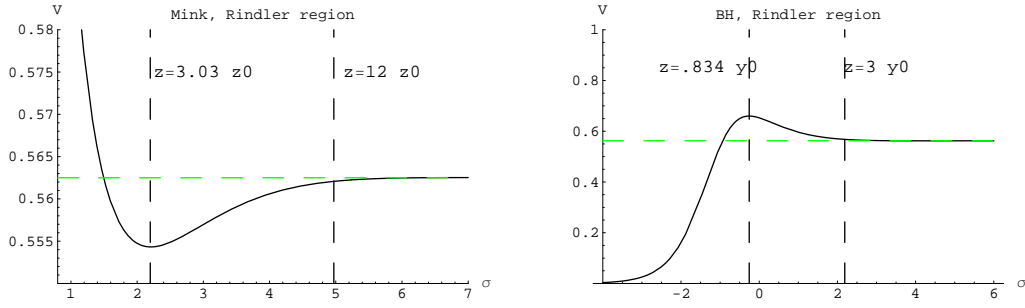


Figure 6: Schrödinger potentials for the D3/D7 vector excitation in Rindler space, as well as an estimate of the left-hand side of the plateau, for the Minkowski and black hole embeddings respectively.

Let us now compute the lengths of the various regions. First, in order to show that the *deep IR region* has a size which is independent of z_0 or y_0 , we make use of the scaling symmetry of (3.8). Suppose that we have a Minkowski solution

$$y = f_1(z), \quad \text{which satisfies } y(\bar{z}_0) = 0, \quad (3.18)$$

i.e. \bar{z}_0 is the point where the brane is closest to the horizon. Using scaling symmetry, there is then another solution

$$y = f_2(z) \equiv f_1\left(z \frac{\bar{z}_0}{z_0}\right) \frac{z_0}{\bar{z}_0}, \quad \text{which satisfies } y(z_0) = 0. \quad (3.19)$$

Next, let us introduce a threshold Δ , which is a fixed and small positive number. When the distance between two branes is smaller than Δ , we will consider them to be coincident. Assume now that we have found a point $z = \bar{z}_{\text{left}}$ for which the distance between the first embedding and the critical one is equal to this Δ ,

$$f_1(\bar{z}_{\text{left}}) - \sqrt{6-p} \bar{z}_{\text{left}} = \Delta. \quad (3.20)$$

This tells us immediately that, at a point $z_{\text{left}} = (\bar{z}_{\text{left}}/\bar{z}_0) z_0$, the distance of the second embedding to the critical one satisfies

$$f_2(z_{\text{left}}) - f_{\text{crit}}(z_{\text{left}}) = f_1\left(z_0 \frac{\bar{z}_{\text{left}}}{\bar{z}_0} \frac{\bar{z}_0}{z_0}\right) \frac{z_0}{\bar{z}_0} - \sqrt{6-p} z_0 \frac{\bar{z}_{\text{left}}}{\bar{z}_0} = \frac{z_0}{\bar{z}_0} \Delta < \Delta \quad \text{if } z_0 < \bar{z}_0. \quad (3.21)$$

In other words: if we define the end of the deep IR region to scale like linearly in z_0 , and if we fix the proportionality constant for some value of z_0 , then the approximation is better for all embeddings which are closer to critical. We can thus define the deep IR region to be $z_0 < z < \Lambda z_0$ for some Λ which is independent of z_0 .

The length of the deep IR region in the Schrödinger coordinate σ now comes out to be independent of z_0 , because $\partial_z y$ is a function of z/z_0 only (this is a consequence of the scaling symmetry). Therefore, using the value of Σ in (3.15), we find

$$\Delta \sigma_{\text{deep IR}}^{\text{Mink}} = \int_{z_0}^{\Lambda z_0} \frac{(1 + Y^2(z/z_0))^{1/2}}{z} dz = \int_1^{\Lambda} \frac{(1 + Y^2(q))^{1/2}}{q} dq, \quad (3.22)$$

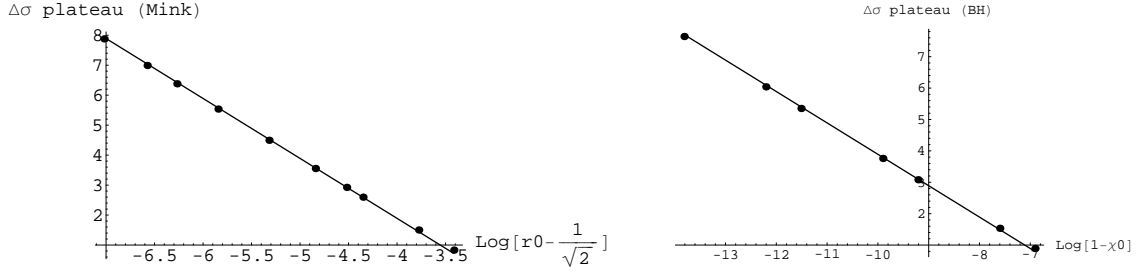


Figure 7: Numerical values (for the D3/D7 system) for the width of the plateau in the Schrödinger σ coordinate, for the Minkowski and black hole embeddings, together with their analytic approximations (3.23) and (3.24).

where $Y(z/z_0) \equiv \partial_z y$. This expression is independent of z_0 . The length of the “intermediate IR” region, $\Lambda z_0 < z < \epsilon R_{\text{Rindler}}$ for some $\epsilon < 1$, can be computed using the critical embedding.

We now concentrate on the D3/D7 case, for which the edges of the plateau are given by $\Lambda \approx 3$ and $\epsilon \approx 1/5$. One finds

$$\Delta\sigma_{\text{plateau}}^{\text{Mink}} \approx \int_{\Lambda z_0}^{\epsilon L} \frac{2}{z} dz = 2 \log \frac{\epsilon L}{\Lambda z_0} \approx -2 \log(r_0 - 1/\sqrt{2}) - 6.11. \quad (3.23)$$

The numerical factors ϵ and Λ are of course somewhat arbitrary, but the scaling with r_0 is fixed by the critical embedding. This scaling is reproduced well by the numerical data, see figure 7a (the black dashed vertical lines in figure 2 indicate the edges of the plateau). Finally, there is a UV region which is out of reach of the Rindler approximation. However, this UV region is similar to the one for zero-temperature embeddings, i.e. has finite size in the Schrödinger coordinate, independent of r_0 .

A similar logic applies to the black hole embeddings. The agreement with the critical embedding (or equivalently, the start of the plateau) again occurs at around $z \approx 3y_0$, and the Rindler approximation breaks down at $z \approx L/5$. We then find that the plateau region scales as

$$\Delta\sigma_{\text{plateau}}^{\text{BH}} \approx \int_{\Lambda y_0}^{\epsilon L} \frac{2}{z} dz = 2 \log \frac{\epsilon L}{\Lambda y_0} \approx -\log(1 - \chi_0) - 6.11, \quad (3.24)$$

Again, this scaling with χ_0 agrees well with the size of the plateau as measured from the numerical data, see figure 7b (the black dashed vertical lines in figure 3 indicate the edges of the plateau). There is also again a UV region, which looks like the UV part of the potential at zero-temperature, which has finite size in the Schrödinger coordinate.

We thus see that in both cases, we can determine the size of the plateau as a function of the distance to the critical embedding. The plateau becomes of infinite length, and all other IR and UV features of the potentials get infinitely pushed away. They remain of finite size, however, and their contributions to the spectrum scale to zero in the critical limit (some

caricature potentials in which this can be seen explicitly are discussed in appendix A.2). Therefore, we conclude that the mass spectrum can be approximated by using a square well potential on the Minkowski side, and a square step when one approaches from the black hole side (see figure 4), where the plateau sizes scale as in (3.23) and (3.24).

3.4 Meson and quasi-normal modes

Having obtained simple potentials for the two types of brane embeddings, let us now look at the spectrum. For the Minkowski embedding, the masses are simply given by the solution of the Schrödinger equation in a box of height V_{crit} . This yields

$$\sqrt{\tilde{\omega}_n^2 - V_{\text{crit}}} \approx \frac{n\pi}{\sigma_{\text{UV}} - \sigma_{\text{IR}}}, \quad n \in \mathbb{N}. \quad (3.25)$$

However, the box size $\sigma_{\text{UV}} - \sigma_{\text{IR}}$ depends on z_0 , and diverges in the critical limit. Thus, all meson masses tend to $\sqrt{V_{\text{crit}}}$, as alluded to in the introduction. Verifying this numerically, on the other hand, is slightly subtle because the masses approach the limit only slowly.

For the black hole embedding, we need to consider a potential with two regions. In the first region, with range $-\infty < \sigma < \sigma_{\text{step}}$, the potential vanishes. The solution of the Schrödinger equation which has incoming boundary conditions at $\sigma = -\infty$ is $\tilde{\psi}_{(1)} = e^{-i\tilde{\omega}\sigma}$. To simplify notation, we will set $\sigma_{\text{UV}} = 0$. In the second region, with range $\sigma_{\text{step}} < \sigma < 0$, the potential has the value given in (3.17). The solution now reads $\tilde{\psi}_{(2)} = A \sin(\sqrt{\tilde{\omega}^2 - V_{\text{crit}}}\sigma)$ where A is a constant to be determined and we have imposed $\tilde{\psi}(\sigma = 0) = 0$ since there is an infinite wall. By matching the values of $\tilde{\psi}$ and its derivative at $\sigma = \sigma_{\text{step}}$, we find a single equation for the values of the quasi-normal frequencies,

$$i\tilde{\omega} \sin(\sqrt{\tilde{\omega}^2 - V_{\text{crit}}}\sigma_{\text{step}}) + \sqrt{\tilde{\omega}^2 - V_{\text{crit}}} \cos(\sqrt{\tilde{\omega}^2 - V_{\text{crit}}}\sigma_{\text{step}}) = 0. \quad (3.26)$$

Given V_{crit} and σ_{step} , one can find numerically the complex values of $\tilde{\omega}$ that solve this equation. However, let us look at a particularly interesting limit,

$$|\sigma_{\text{step}}| \sqrt{V_{\text{crit}}} \gg 1. \quad (3.27)$$

Since in our problem V_{crit} is fixed to be the constant in (3.17), this is satisfied for large (negative) σ_{step} . Remembering that $|\sigma_{\text{step}}|$ grows unbounded when the flavour brane approaches the critical embedding ($y_0 \rightarrow 0$), this is in fact the limit in which we are interested. But now we can obtain $\tilde{\omega}$ as an expansion in $(\sigma_{\text{step}} \sqrt{V_{\text{crit}}})^{-1}$,

$$\tilde{\omega}_n = \sqrt{V_{\text{crit}}} \left(\pm 1 \pm \frac{n^2 \pi^2}{2\sigma_{\text{step}}^2 V_{\text{crit}}} + iF \frac{n^2 \pi^2}{\sigma_{\text{step}}^3 V_{\text{crit}}^{\frac{3}{2}}} + \mathcal{O}\left((\sigma_{\text{step}} \sqrt{V_{\text{crit}}})^{-4}\right) \right), \quad n \in \mathbb{N}. \quad (3.28)$$

Here F is the first coefficient in this expansion which depends on the finite-size details of the potential; for the step potential of figure 4 we have $F = 1$ (for details see appendix A.2).

This expression is rather appealing. The real part is the one obtained if one had an IR infinite wall at σ_{step} . That is, it corresponds to the meson masses of the Minkowski embedding if one identifies σ_{step} with σ_{IR} there. In fact, from figures 2 and 3 we see that

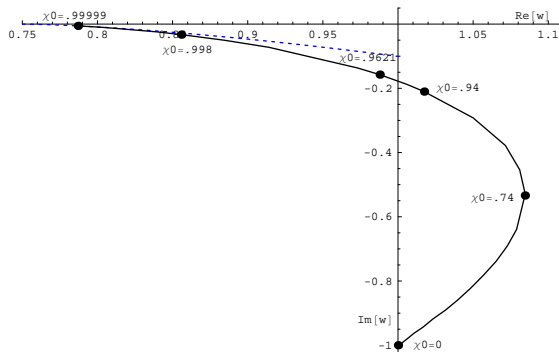


Figure 8: Behaviour of the first quasi-normal mode of the D3/D7 system with a black hole embedding, as a function of the distance χ_0 to the critical embedding. The blue dotted line represents the analytic result obtained by using a step potential (where $F = 0.84$ was used in (3.28)). The values $\chi_0 = 0.94$ and $\chi_0 = 0.9621$ correspond to the points where the embedding becomes metastable and unstable, respectively.

these values are comparable if z_0 and y_0 are of the same order. On top of that, there is a small, negative imaginary part (remember $\sigma_{\text{step}} < 0$).

The numerical analysis of the quasi-normal frequency spectrum away from the critical embedding, as presented in [4] for a scalar excitation, requires some care if one wants to extend it to the regime of near-critical embeddings. In the coordinates used here, we found reliable numerical results for the first quasi-normal mode, which match smoothly onto our analytic results. The result for the D3/D7 system is shown in figure 8. Equation (3.28) thus provides us with an endpoint for the vector analog of the spiralling trajectories of the quasi-normal modes shown in figure 4 of [4].

Summarising the present section, we have seen that any finite number of meson masses in the D3/D7 system come down to a single value $\sqrt{V_{\text{crit}}}$. Similarly, any finite number of quasi-normal modes come down to the same value as the critical embedding is approached from the black hole phase. Since the masses and quasi-normal modes are labelled by a single excitation number n , there is in principle an infinite number of ways to relate the states in these two spectra, and the connection between mesons and quasi-normal modes thus seems more subtle than previously suggested [5, 6]. Note that the degeneracy is not in contradiction with the Von Neumann & Wigner theorem [13]. In our case, a finite change of the parameter (here given by T/m_q) leads to an infinite change of the potential (the logarithmic growth which diverges at the critical embedding), while the Von Neumann & Wigner theorem requires the potential to change smoothly.

4. The D4/D8 system

4.1 Schrödinger potentials

The D4/D8 embeddings used in the Sakai-Sugimoto model are different from the cases analysed so far. Instead of being described by a curve in the $r - \lambda$ plane, these embeddings are given by curve in the $u - \tau$ subspace, i.e. these are more like the “equatorial embeddings”

of the D3/D7 system. There is a family of Minkowski-type embeddings, labelled by the lowest point u_0 of the D8 brane in the u -direction. The black hole embeddings are labelled by the distance in the τ direction between the two halves of the D8 brane, but this distance is a modulus and the spectrum is independent of it.

In the intermediate-temperature phase, where chiral symmetry is broken, the vector meson fluctuation equation reads [10] (we set $u_T = L = 1$ from now on)

$$\partial_u \left(u^{5/2} \gamma^{-1/2} f_4(u)^{1/2} \partial_u \psi_{(n)} \right) + u^{-1/2} \gamma^{1/2} f_4(u)^{-1/2} \tilde{m}_{(n)}^2 \psi_{(n)} = 0. \quad (4.1)$$

where

$$\gamma = \frac{u^8}{u^8 f_4(u) - u_0^8 f_4(u_0)}. \quad (4.2)$$

Following the by now familiar procedure we thus construct the Schrödinger radial variable σ through

$$\sigma(u) = \pm \int_{u_0}^u \frac{u^4 du}{\sqrt{u^3 - 1} \sqrt{u^5(u^3 - 1) - u_0^5(u_0^3 - 1)}}. \quad (4.3)$$

We have defined $\sigma = 0$ as the tip of the brane ($u = u_0$) and the two signs correspond to the two branches of the brane worldvolume. For any $u_0 > 1$, it is clear that $\sigma_{\max} = \sigma(u = \infty)$ is finite, so σ lives in a finite range. However, as $u_0 \rightarrow 1$, σ_{\max} diverges. The rate of divergence can be computed by making a coordinate change $\delta = (u/u_0)^3 - 1$, which leads to

$$\sigma_{\max}(\epsilon) = \frac{1}{3} \int_0^\infty \frac{(1 + \delta)^{-\frac{1}{6}}}{\sqrt{\delta} \sqrt{\delta + \epsilon}} d\delta, \quad \text{where} \quad \epsilon = 1 - u_0^{-3}. \quad (4.4)$$

This integral can be evaluated by splitting it into two regions, $0 < \delta < \sqrt{\epsilon}$ and $\sqrt{\epsilon} < \delta < \infty$. This leads to two integrals which can be evaluated analytically, up to corrections which vanish as $\sqrt{\epsilon}$. The result is

$$\sigma_{\max}(\epsilon) = \frac{1}{6} \left(\sqrt{3}\pi + 8 \log 2 + \log 3 - 2 \log(u_0 - 1) \right) + \mathcal{O}(\sqrt{\epsilon}). \quad (4.5)$$

The Schrödinger potential in the u -variable is:

$$V = \frac{u^5(2u^6 + 2u^3 - 4) + u_0^5(u_0^3 - 1)(6u^3 - 9)}{4u^{10}}. \quad (4.6)$$

Its limiting behaviour at the tip and far away from it is given by

$$V(u = u_0) = \frac{8u_0^6 - 13u_0^3 + 5}{4u_0^5}, \quad V(u \rightarrow \infty) = \infty. \quad (4.7)$$

The dependence of V on the σ variable can be computed numerically. The result for various values of u_0 is plotted in figure 9. These plots suggest that it should be possible to find two square well potentials, which provide an upper resp. lower bound on the potential. The lower bound is obtained by using a width which is twice the expression (4.5) (the red dashed outer box in figure 9).

For the width of the upper bound potential, we pick a point σ_i on the σ axis for which we can show that the potential goes to zero in the limit $u_0 \rightarrow 1$, and which is such

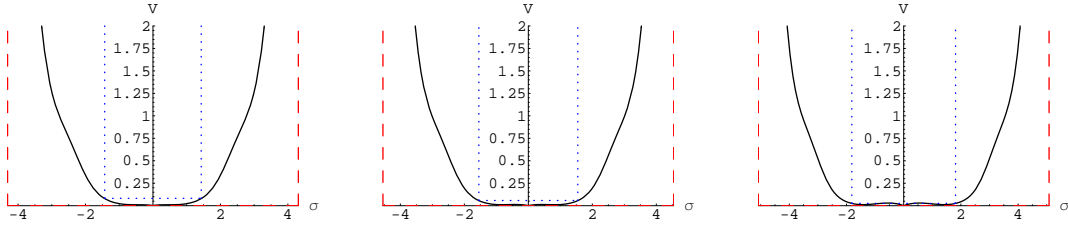


Figure 9: The Schrödinger potential for the Sakai-Sugimoto system in the phase with broken chiral symmetry, for various decreasing values of the position u_0 of the tip of the brane. The dashed red lines (outer box) denote the potential used for the computation of the lower bound, while the dotted black lines (inner box) denote the potential for the upper bound (with $q = 2$).

that $\sigma_i \rightarrow \infty$ in this limit. A suitable point is defined by $\delta = \epsilon^{1/q}$ for some positive q . This point satisfies

$$\sigma_i = \frac{1}{3} \int_0^{\epsilon^{1/q}} \frac{1}{\sqrt{\delta}\sqrt{\delta+\epsilon}} d\delta = \frac{2}{3} \log 2 - \frac{q-1}{3q} \log \epsilon + \mathcal{O}(\epsilon^{\frac{q-1}{q}}). \quad (4.8)$$

The potential $V(\sigma_i)$ behaves as $\mathcal{O}((u_0 - 1)^{1/q})$ and thus goes to zero. For sufficiently small u_0 the potential is monotonic, and thus we conclude that $V(\sigma < \sigma_i)$ goes to zero as well. Furthermore, we can take the formal limit $q \rightarrow \infty$ in (4.8). In this limit, the box size again diverges logarithmically as $u_0 \rightarrow 1$, with the same coefficient of the logarithm as in (4.5). We will use a box with width twice that of (4.8) for $q \rightarrow \infty$ to obtain an upper bound to the potential (the black dashed inner box in figure 9).

In the phase where chiral symmetry is restored, the vector meson fluctuations are governed by the equation

$$-u^{1/2}(1-u^{-3})\partial_u\left(u^{5/2}(1-u^{-3})\partial_u\psi(u)\right) = \tilde{\omega}^2\psi(u). \quad (4.9)$$

A Schrödinger equation is obtained by using

$$\Gamma = \frac{1}{u^{1/2}(1-u^{-3})}, \quad \Sigma = \frac{1}{u^{3/2}(1-u^{-3})}, \quad \Xi = u^{1/2}, \quad \tilde{\psi} = \Xi\psi. \quad (4.10)$$

The Schrödinger coordinate, obtained using $d\sigma/du = \Sigma$, is a complicated function of u which does not admit a simple inverse. We therefore restrict to a numerical plot of the potential in figure 10. In the u coordinate it is given by

$$V = \frac{u^6 + u^3 - 2}{2u^5}. \quad (4.11)$$

This potential is quite featureless and we will hence resort to a numerical determination of the quasi-normal mode spectrum for the D4/D8 case (this potential is similar to the one for the equatorial D3/D7 embedding).

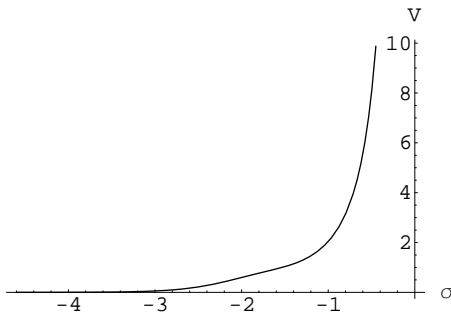


Figure 10: The Schrödinger potential for the Sakai-Sugimoto system in the phase where chiral symmetry is restored. The σ coordinate spans the half-line $-\infty < \sigma < 0$.

4.2 Mesons and quasi-normal modes

Using the square well potentials which we have shown in the previous section to be upper resp. lower bounds for the full Sakai-Sugimoto potential, it is easy to compute the mass spectrum in the $u_0 \rightarrow 1$ limit. From the box with a width given by twice (4.5) we find

$$\tilde{m}_{(n)}(u_0) \gtrsim \frac{n\pi}{2 \left(\frac{\sqrt{3}\pi}{6} + \frac{4}{3} \log 2 + \frac{1}{6} \log 3 - \frac{1}{3} \log(u_0 - 1) \right)}, \quad n \in \mathbb{N}, \quad (4.12)$$

whereas the box with width given by twice (4.8) we get

$$\tilde{m}_{(n)}(u_0) \lesssim \frac{n\pi}{2 \left(\frac{2}{3} \log 2 - \frac{1}{3} \log 3 - \frac{1}{3} \log(u_0 - 1) \right)}, \quad n \in \mathbb{N}. \quad (4.13)$$

To re-instate the L and u_T dependence, note that

$$\tilde{m} = \frac{L^{3/2}}{u_T^{1/2}} m = \frac{3m}{4\pi T}. \quad (4.14)$$

These expressions both go to zero as $u_0 \rightarrow 1$; see figure 11 for a comparison with the numerically determined spectrum.

Because the potential in the high-temperature phase (4.11) does not take a simple form, we again have to resort to numerics in order to find the quasi-normal mode spectrum. The first six vector meson masses are given in figure (12) (each of these is twofold degenerate because of chiral symmetry). A fit to a linear function yields

$$\tilde{\omega}_n = \pm(0.31 + 1.305n) - (0.145 + 0.752n)i, \quad (4.15)$$

(where $\tilde{\omega}$ is related to ω by a relation similar to (4.14)). The numbers agree with the analysis presented in [21].

Comparing the real parts of the quasi-normal modes with the meson masses in the intermediate-temperature regime, we see that there is no room to connect the two in a smooth way. The masses of any finite number of mesons come down to zero as the critical, overheated embedding is approached. In contrast to this, the quasi-normal modes take values which are equally spaced in the complex plane, with a lower bound on the real part which is non-zero. An identification along the lines of [5, 6] thus does not seem possible for the Sakai-Sugimoto model.

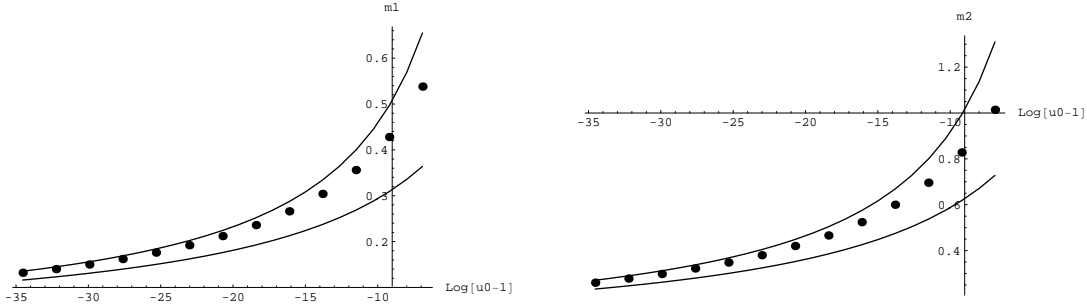


Figure 11: The first vector (left) and axial vector (right) meson masses computed numerically, versus the analytic upper and lower bounds computed (4.13) and (4.12).

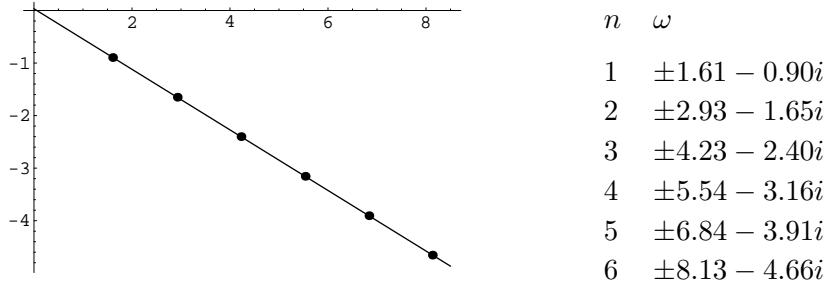


Figure 12: The spectrum of the first twelve quasi-normal vector modes of the chirally symmetric phase of the Sakai-Sugimoto model (each mode is twofold degenerate because of chiral symmetry).

5. Conclusions and discussion

We have analysed the form of the Schrödinger potential for vector meson fluctuations in various holographic duals to gauge theories with matter. These potentials exhibit some generic structure which we expect to see for more general classes of models. In the Rindler region, a Minkowski embedding will lead to a box-shaped potential, while a black hole embedding will lead to a step. When no Rindler approximation can be made, which is the case for the equatorial embeddings, more of the background can be seen, and the potential is typically more complicated.

In the non-equatorial type transition of the D3/D7 system, we have shown how any finite number of meson masses come down to a fixed value. Similarly, when the embedding is approached from the black hole side, any finite number of quasi-normal modes approaches this same value. Lacking any quantum numbers to distinguish them, the connection between these spectra is thus more subtle than previously suggested.¹⁰

¹⁰In [5] it was observed that peaks appear in the spectral function, which is consistent with our results. However, our calculations show that these peaks all converge on $\tilde{\omega} = 0.75$. The spectra are symmetric only for the artificial choice of fixed z_0/y_0 .

For the D4/D8 embeddings (“equatorial”), we have shown that all meson masses come down to zero. This is consistent with the fact that there is a proper chiral symmetry restoration after the transition, in sharp contrast to the D3/D7 system. The quasi-normal mode spectrum, on the other hand, is equally-spaced with a non-zero lowest frequency mode. This result does not support the idea that quasi-normal modes are continuously connected to meson modes. It is conceivable that, if one would introduce a bare quark mass into the Sakai-Sugimoto model (along the lines of [22–24]), its behaviour would be more similar to the D3/D7 case. It would also be interesting to verify if the qualitative results we have obtained for the D4/D8 model are realised in its non-critical version [25], whose thermal phase structure was analysed in [26].

We have not yet touched the issue of chemical potentials. In the presence of a baryon chemical potential, the spectral function exhibits, for large enough m_q/T , sharp peaks close to the critical embedding [6]. Moreover, these peaks converge on the meson masses for the Minkowski embeddings. However, while the embeddings for large chemical potential are very close to the Minkowski embeddings (and hence the agreement in the spectrum), they are not related to each other by a small deformation in the gauge theory parameter space. The situation is reminiscent of a strong/weak duality in chemical potential. It would be interesting to understand this behaviour for isospin potentials as well [27].

Acknowledgements

We thank Ofer Aharony for extensive comments on the draft, and Johanna Erdmenger, Nick Evans and Andrei Starinets for discussions. The work of AP & KP was supported by VIDI grant 016.069.313 from the Dutch Organisation for Scientific Research (NWO). The work of AP is also partially supported by EU-RTN network MRTN-CT-2004-005104 and INTAS contract 03-51-6346.

A. Appendix

A.1 Coordinate frames

We collect here a number of technical details related to the coordinate choices made in the main text. We will rewrite the metric (2.1) in two different ways, as depicted in figure 1. One coordinate frame is better adapted for computations with Minkowski embeddings, while the other one is more suitable for black hole embeddings.

The first step is to define coordinates such that the second part of the metric (2.1) becomes conformally flat. This is achieved with

$$u = u_T \left(\tilde{\rho}^{\frac{7-p}{2}} + \frac{1}{4\tilde{\rho}^{\frac{7-p}{2}}} \right)^{\frac{2}{7-p}}, \quad K_p(\tilde{\rho}) = \frac{u^{\frac{p-3}{2}}}{\tilde{\rho}^2}. \quad (\text{A.1})$$

The metric (2.1) becomes

$$ds^2 = \left(\frac{u}{L} \right)^{\frac{7-p}{2}} \left(-f_p dt^2 + \delta_{ij} dx^i dx^j \right) + L^{\frac{7-p}{2}} K_p(\tilde{\rho}) \left(d\tilde{\rho}^2 + \tilde{\rho}^2 d\Omega_{8-p}^2 \right). \quad (\text{A.2})$$

We can reexpress the flat factor inside the last bracket by defining $\tilde{\rho}^2 = r^2 + \lambda^2$, and we get

$$ds^2 = \left(\frac{u}{L}\right)^{\frac{7-p}{2}} \left(-f_p dt^2 + \delta_{ij} dx^i dx^j\right) + L^{\frac{7-p}{2}} K_p \left(d\lambda^2 + \lambda^2 d\Omega_{6-p}^2 + dr^2 + r^2 d\phi^2\right). \quad (\text{A.3})$$

This is the $r - \lambda$ system depicted in figure 1, and for $p = 4$, it corresponds to the coordinate system defined in [2]. We have found this frame convenient to numerically analyse the Minkowski embeddings which reach $\lambda = 0$ at some $r = r_0$, which parametrises the one-parameter family of embeddings (Schrödinger potentials for various values of r_0 in the D3/D7 case are plotted in figure 2). The critical embedding corresponds to $r_0 = 2^{\frac{2}{p-7}}$.

We now define a $\rho - \chi$ coordinate system (as shown in figure 1) following [17]. We first rescale the ρ coordinate defined above as:

$$\rho = 2^{\frac{2}{7-p}} \tilde{\rho}, \quad (\text{A.4})$$

such that the horizon is at $\rho = 1$ and write the metric of the sphere as $d\Omega_{8-p} = d\theta^2 + \sin^2 \theta d\Omega_{6-p} + \cos^2 \theta d\phi^2$. If we now define $\chi = \cos \theta$, we get

$$ds^2 = \left(\frac{u}{L}\right)^{\frac{7-p}{2}} \left(-f_p dt^2 + \delta_{ij} dx^i dx^j\right) + L^{\frac{7-p}{2}} u^{\frac{p-3}{2}} \left(\frac{d\rho^2}{\rho^2} + \frac{d\chi^2}{1-\chi^2} + (1-\chi^2) d\Omega_{6-p}^2 + \chi^2 d\phi^2\right), \quad (\text{A.5})$$

where u should be understood to be a function of ρ . This coordinate system is convenient to study the black hole embeddings, parametrised by $\chi_0 \equiv \chi|_{\rho=1}$ (with $\chi_0 = 1$ being the critical embedding). Some Schrödinger potentials for various values of χ_0 in the D3/D7 case are shown in figure 3. In this set of coordinates, Minkowski embeddings are parametrised by $\rho_0 \equiv \rho|_{\chi=1}$. For embeddings near the critical one, there are simple relations between these parameters and y_0, z_0 as defined in section 3.2. For the D3/D7 case ($p = n = 3$), they read:

$$y_0 = \sqrt{2}\sqrt{1-\chi_0} L (1 + \mathcal{O}(1-\chi_0)) \quad z_0 = L (\rho_0 - 1) (1 + \mathcal{O}(\rho_0 - 1)) \quad (\text{A.6})$$

These relations, together with $\rho_0 = \sqrt{2}r_0$, were used to obtain the last equality in equations (3.23) and (3.24).

A.2 Quasinormal frequencies in toy potentials

We have argued in the main text that for the D3/D7 and D4/D6 cases near the critical embedding, the Schrödinger potential presents a plateau of diverging width in the σ -coordinate. At its edges, there are some IR and UV features which remain of finite size. Since the plateau is infinitely big as compared to these finite size details, one expects that these details only affect the quasinormal frequencies (or meson masses) in a subleading way. In this appendix, we will explicitly check this for two toy Schrödinger potentials that approximate the near critical Schrödinger potential for D3/D7 black hole embeddings.

By looking at the plots in figure 3, one sees that there is a bump before the plateau and a dip after the plateau, before the infinite wall. We stress that the size of the bump and dip remain constant as the plateau grows unbounded when the embedding approaches the critical one. Let us, accordingly, consider the following approximation for the Schrödinger potential which we insert in (2.9):

$$\begin{aligned}
V &= 0 && \text{for } \sigma < \sigma_{\text{step}} + x_1, \\
V &= V_{\text{crit}} + h_1 && \text{for } \sigma_{\text{step}} + x_1 < \sigma < \sigma_{\text{step}}, \\
V &= V_{\text{crit}} && \text{for } \sigma_{\text{step}} < \sigma < x_2, \\
V &= V_{\text{crit}} - h_2 && \text{for } x_2 < \sigma < 0,
\end{aligned} \tag{A.7}$$

and an infinite wall at $\sigma = 0$. We want to consider $V_{\text{crit}}, h_1, h_2 > 0$ and $\sigma_{\text{step}}, x_1, x_2 < 0$, in a limit $\sigma_{\text{step}} \rightarrow -\infty$ with $V_{\text{crit}}, h_1, h_2, x_1, x_2$ fixed. We can obtain a solution of the Schrödinger problem with IR incoming boundary conditions ($\tilde{\psi} = e^{-i\omega\sigma}$ in region 1) as a series in $\frac{1}{\sigma_{\text{step}}\sqrt{V_{\text{crit}}}}$. The solution is the same as in the simple step potential, see (3.28), with F depending on the various parameters,

$$\begin{aligned}
F &= -i \left(\sqrt{h_1 h_2 V_{\text{crit}}} \cosh(\sqrt{h_1 x_1}) - i h_1 \sqrt{h_2} \sinh(\sqrt{h_1 x_1}) \right)^{-1} \\
&\times \left(\cosh(\sqrt{h_1 x_1}) \left[\sqrt{h_1 h_2 V_{\text{crit}}} x_2 + i \sqrt{h_1 h_2 V_{\text{crit}}} - \sqrt{h_1} V_{\text{crit}} \tan(\sqrt{h_2} x_2) \right] \right. \\
&\quad \left. + \sinh(\sqrt{h_1 x_1}) \left[-i h_1 \sqrt{h_2 V_{\text{crit}}} x_2 - \sqrt{h_2} V_{\text{crit}} + i h_1 \sqrt{V_{\text{crit}}} \tan(\sqrt{h_2} x_2) \right] \right).
\end{aligned} \tag{A.8}$$

If we insert $h_1 = h_2 = .1$, $x_1 = x_2 = -2$, which is approximately appropriate for the potentials we are dealing with, and also use $V_{\text{crit}} = 9/16$, we get: $F \approx .65 - 1.72i$.

One may also worry if the exponential tail of the Schrödinger potentials, which is proportional to $e^{2\sigma}$ as $\sigma \rightarrow -\infty$ could affect the computation. Let us address this point by considering another toy potential slightly more complicated than the one in figure 4:

$$\begin{aligned}
V &= V_{\text{crit}} e^{2\sigma - 2\sigma_{\text{step}}} && \text{for } \sigma < \sigma_{\text{step}}, \\
V &= V_{\text{crit}} && \text{for } \sigma_{\text{step}} < \sigma < 0,
\end{aligned} \tag{A.9}$$

Again, one can make an expansion for the $\sigma_{\text{step}} \rightarrow -\infty$ limit and the solution for the quasinormal frequencies is again (3.28) where F now can be written in terms of the modified Bessel function:

$$F = \frac{-2i I_{-i\sqrt{V_{\text{crit}}}}(\sqrt{V_{\text{crit}}})}{I_{-1-i\sqrt{V_{\text{crit}}}}(\sqrt{V_{\text{crit}}}) + I_{1-i\sqrt{V_{\text{crit}}}}(\sqrt{V_{\text{crit}}})} \tag{A.10}$$

If we insert $V_{\text{crit}} = 9/16$, we find $F \approx 1.1 - .32i$.

These two examples explicitly show how in the $\sigma_{\text{step}} \rightarrow -\infty$ limit, the details of the potential only appear in $\tilde{\omega}_{(n)}$ at order $(\sigma_{\text{step}}\sqrt{V_{\text{crit}}})^{-3}$ (which is however the leading imaginary part for the quasinormal frequencies). In summary, this shows that finite details do not change the discussion based on the infinite plateau.

References

- [1] J. Babington, J. Erdmenger, N. J. Evans, Z. Guralnik, and I. Kirsch, “Chiral symmetry breaking and pions in non-supersymmetric gauge/gravity duals”, *Phys. Rev. D* **69** (2004) 066007, [hep-th/0306018](#).
- [2] M. Kruczenski, D. Mateos, R. C. Myers, and D. J. Winters, “Towards a holographic dual of large- N_c QCD”, *JHEP* **05** (2004) 041, [hep-th/0311270](#).
- [3] O. Aharony, J. Sonnenschein, and S. Yankielowicz, “A holographic model of deconfinement and chiral symmetry restoration”, *Ann. Phys.* **322** (2007) 1420–1443, [hep-th/0604161](#).
- [4] C. Hoyos-Badajoz, K. Landsteiner, and S. Montero, “Holographic meson melting”, *JHEP* **04** (2007) 031, [hep-th/0612169](#).
- [5] R. C. Myers, A. O. Starinets, and R. M. Thomson, “Holographic spectral functions and diffusion constants for fundamental matter”, *JHEP* **11** (2007) 091, [arXiv:0706.0162 \[hep-th\]](#).
- [6] J. Erdmenger, M. Kaminski, and F. Rust, “Holographic vector mesons from spectral functions at finite baryon or isospin density”, [arXiv:0710.0334 \[hep-th\]](#).
- [7] K. Peeters, J. Sonnenschein, and M. Zamaklar, “Holographic decays of large-spin mesons”, *JHEP* **02** (2006) 009, [hep-th/0511044](#).
- [8] **QCD-TARO** Collaboration, P. de Forcrand *et al.*, “Meson correlators in finite temperature lattice QCD”, *Phys. Rev. D* **63** (2001) 054501, [hep-lat/0008005](#).
- [9] M. B. Oktay, M. J. Peardon, J. I. Skullerud, G. Aarts, and C. R. Allton, “Charmonium properties in the quark-gluon plasma”, *PoS LAT2007* (2007) 227, [arXiv:0710.2795 \[hep-lat\]](#).
- [10] K. Peeters, J. Sonnenschein, and M. Zamaklar, “Holographic melting and related properties of mesons in a quark gluon plasma”, *Phys. Rev. D* **74** (2006) 106008, [hep-th/0606195](#).
- [11] F. Karsch, “Lattice QCD at finite temperature and density”, *Nucl. Phys. Proc. Suppl.* **83** (2000) 14–23, [hep-lat/9909006](#).
- [12] S. A. Gottlieb *et al.*, “Thermodynamics of lattice QCD with two light quark flavours on a $16^3 \times 8$ lattice. II”, *Phys. Rev. D* **55** (1997) 6852–6860, [hep-lat/9612020](#).
- [13] J. von Neumann and E. Wigner, “On the behavior of eigenvalues in adiabatic processes”, *Z. Phys.* **30** (1929) 467–470.
- [14] E. Schreiber, “Excited mesons and quantization of string endpoints”, [hep-th/0403226](#).

- [15] M. Kruczenski, D. Mateos, R. C. Myers, and D. J. Winters, “Meson spectroscopy in AdS/CFT with flavour”, *JHEP* **07** (2003) 049, [hep-th/0304032](#).
- [16] V. P. Frolov, A. L. Larsen, and M. Christensen, “Domain wall interacting with a black hole: A new example of critical phenomena”, *Phys. Rev.* **D59** (1999) 125008, [hep-th/9811148](#).
- [17] D. Mateos, R. C. Myers, and R. M. Thomson, “Holographic phase transitions with fundamental matter”, *Phys. Rev. Lett.* **97** (2006) 091601, [hep-th/0605046](#).
- [18] K. Peeters and M. Zamaklar, “Dissociation by acceleration”, *JHEP* **01** (2007) 038, [arXiv:0711.3446 \[hep-th\]](#).
- [19] D. Mateos, R. C. Myers, and R. M. Thomson, “Thermodynamics of the brane”, *JHEP* **05** (2007) 067, [hep-th/0701132](#).
- [20] G. T. Horowitz and V. E. Hubeny, “Quasinormal modes of AdS black holes and the approach to thermal equilibrium”, *Phys. Rev.* **D62** (2000) 024027, [hep-th/9909056](#).
- [21] N. Evans and E. Threlfall, “Mesonic quasinormal modes of the Sakai-Sugimoto model at high temperature”, [arXiv:0802.0775 \[hep-th\]](#).
- [22] O. Bergman, S. Seki, and J. Sonnenschein, “Quark mass and condensate in HQCD”, *JHEP* **12** (2007) 037, [arXiv:0708.2839 \[hep-th\]](#).
- [23] A. Dhar and P. Nag, “Sakai-Sugimoto model, Tachyon Condensation and Chiral symmetry Breaking”, *JHEP* **01** (2008) 055, [arXiv:0708.3233 \[hep-th\]](#).
- [24] R. Casero, E. Kiritsis, and A. Paredes, “Chiral symmetry breaking as open string tachyon condensation”, *Nucl. Phys.* **B787** (2007) 98–134, [hep-th/0702155](#).
- [25] R. Casero, A. Paredes, and J. Sonnenschein, “Fundamental matter, meson spectroscopy and non-critical string/gauge duality”, *JHEP* **01** (2006) 127, [hep-th/0510110](#).
- [26] V. Mazu and J. Sonnenschein, “Non critical holographic models of the thermal phases of QCD”, [arXiv:0711.4273 \[hep-th\]](#).
- [27] O. Aharony, K. Peeters, J. Sonnenschein, and M. Zamaklar, “Rho meson condensation at finite isospin chemical potential in a holographic model for QCD”, *JHEP* **082** (2007) 1007, [arXiv:0709.3948 \[hep-th\]](#).